JOURNAL OF THEORETICAL
AND APPLIED MECHANICS
63, 3, pp. 491–499, Warsaw 2025
https://doi.org/10.15632/jtam-pl/201313

ESTIMATING EQUIBIAXIAL STRESS-STRAIN RELATION BASED ON NON-HOMOGENEOUS BIAXIAL MEASUREMENT

Kristóf HAVASI, Attila KOSSA*

Department of Applied Mechanics, Faculty of Mechanical Engineering,
Budapest University of Technology and Economics, Műegyetem rkp. 3., H-1111 Budapest, Hungary
*corresponding author, *kossa@mm.bme.hu*

This study investigates the influence of geometry on stress distributions in equibiaxial testing of rubber-like materials using hyperelastic models. Two geometries were examined, characterized by parameters specifying configurations like corner angles and normalized radii. A finite element approach was employed to simulate deformation under equibiaxial stretching, revealing non-homogeneous stress states. Apparent stress ratios were derived to evaluate geometry-induced deviations from purely equibiaxial stress-strain behavior. Results highlight the significance of geometrical factors in stress distributions. The findings offer insights for optimizing specimen designs for equibiaxial material characterization and improving the accuracy of extracted material properties.

Keywords: equibiaxial testing; hyperelastic materials; specimen geometry; finite element analysis; stress-strain relationship.

1. Introduction

The execution of equibiaxial material testing for rubber-like materials remains a challenging task even today, whether involving symmetric or asymmetric biaxial measurements. Such tests frequently utilize so-called cruciform test specimens, but the exact geometry of these specimens remains a subject of debate. There is no consensus or standardized shape; thus, researchers typically design their own specimen geometries for their experiments. To illustrate the wide variety of specimen geometries reported in the literature, we highlight several characteristic designs in the following paragraph.

Perhaps the simplest design is a basic cruciform shape with rectangular arms (Labus & Puttlitz, 2016; Avanzini & Battini, 2016). A more complex variation involves angling the arms at a certain degree (Avanzini & Battini, 2016). However, the corners act as stress concentration regions, and localized rounding can help reduce high stresses in these domains (Bertin *et al.*, 2015). A further refinement involves continuous rounding between the arms, reducing stress concentration effects over a wider section (Jiang *et al.*, 2022; Chen *et al.*, 2013; Seibert *et al.*, 2014; Palacios, Pineda *et al.*, 2017; Avanzini & Battini, 2016; Silberstein *et al.*, 2011). Introducing a central cutout in the specimen allows larger and more visually apparent deformations to be measured (Hartmann *et al.*, 2018; Ranjan *et al.*, 2023). Extending these cutouts toward

Ministry of Science and Higher Education
Republic of Poland

The publication has been funded by the Polish Ministry of Science and Higher Education under the Excellent Science II programme "Support for scientific conferences".
The content of this article was presented during the 40th Danubia-Adria Symposium on Advances in Experimental Mechanics, Gdańsk, Poland, September 24–27, 2024.

the corners can create a more homogeneous stress field (Hartmann *et al.*, 2018; Makinde *et al.*, 1992). If the goal is to ensure that tensile loading is dominant along the arms, notches can be introduced to minimize deformation in the transverse direction (Avanzini & Battini, 2016; Kuwabara *et al.*, 1998). Another approach to reduce transverse deformation in the arms is to incorporate larger incisions rather than small notches (Zhao *et al.*, 2014). These can be combined with a central cutout extending toward the incisions (Hartmann *et al.*, 2018; Makinde *et al.*, 1992). To facilitate easier clamping, head sections can be added to the ends of the arms, tapering toward their intersection (Putra *et al.*, 2020). The tapering can also vary and need not form parallel arm edges in the geometry, potentially featuring a continuously changing shape that helps concentrate stresses in the central region (Palacios-Pineda *et al.*, 2017; Lamkanfi *et al.*, 2015). A middle-way solution involves adding cutouts to a continuously rounded design, focusing the effects more distinctly on the central region of the specimen (Morris *et al.*, 2020). An alternative method is to design the head sections with rounded edges instead of straight sides (Vitucci, 2024). For testing scenarios with low force measurements, thinner arms can be advantageous, as their stress distribution becomes less influential (Seibert *et al.*, 2014). Similar specimen designs can also be used for failure mode investigations, such as specimens with a central notch (Marano *et al.*, 2010) or a central hole to concentrate forces and stresses toward the corners (Oliveira *et al.*, 2021; Hamdoun & Mahnken, 2024). It should also be noted that asymmetric specimens can be used for testing purposes, not just symmetric ones (Chen *et al.*, 2023). The geometries found in the cited articles are illustrated in Fig. 1. For each specimen under biaxial loading the center region, often called a Region of Interest (ROI), shows a certain stress distribution typical for the specimen in use that approximates the pure equibiaxial stress-strain relationship (Chen *et al.*, 2013; Seibert *et al.*, 2014; Morris *et al.*, 2020). It can be concluded that the shapes of these specimens have a great impact on the exact stress fields forming in the material due to the applied loads, thus it would be possible to characterize the effects of the specimen geometries and use this information to grasp the equibiaxial behavior of the experiments carried out.

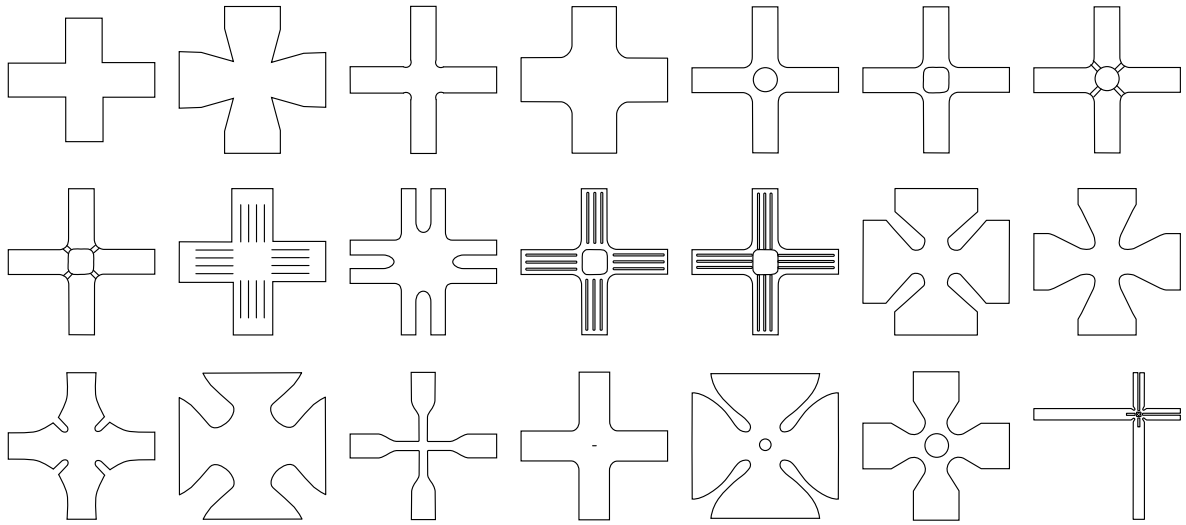

Fig. 1. Illustration of different biaxial test specimen geometries.

As demonstrated, a wide variety of test specimens can be proposed, each tailored to the experimental equipment available to the researcher and the specific properties to be measured. However, it is not possible to identify a globally optimal specimen design that universally satisfies all research needs. As a result, specially designed specimen geometries created to meet specific experimental needs are still widely used.

2. Description of the mechanical problem

In the present study, we investigate two distinct geometries of equibiaxial test specimens, as illustrated in Fig. 2. For both types, the overall dimensions of the specimen form a square with a side length of $3L$, while the ROI is defined by a square with a side length of L located at the center of the specimen. Both geometries are characterized by a single parameter. In the case of the specimen depicted in Fig. 2a, the defining parameter is the angle α as marked in the figure, whereas for the specimen shown in Fig. 2b, the characteristic geometrical parameter is the dimensionless ratio $\beta = R/L$. By varying the parameters α and β, we can generate specimens with different geometrical configurations. The thickness of all specimens is denoted as t. Given that thin specimens are examined, the stress distribution is assumed to be constant along the thickness direction, reducing the original three-dimensional problem to a two-dimensional analysis. For both geometric configurations, we investigate 10 distinct cases, which are identified using a specific coding scheme detailed in Table 1. This table also provides the characteristic geometrical dimensions associated with each code. It is noteworthy that for the geometry coded as B, the case $\beta = 0$ corresponds to case A00; therefore, it is not examined separately. In total, we analyze 20 different specimen geometries (see Fig. 3), enabling us to obtain a comprehensive understanding of how geometry influences the stress distribution in both configurations.

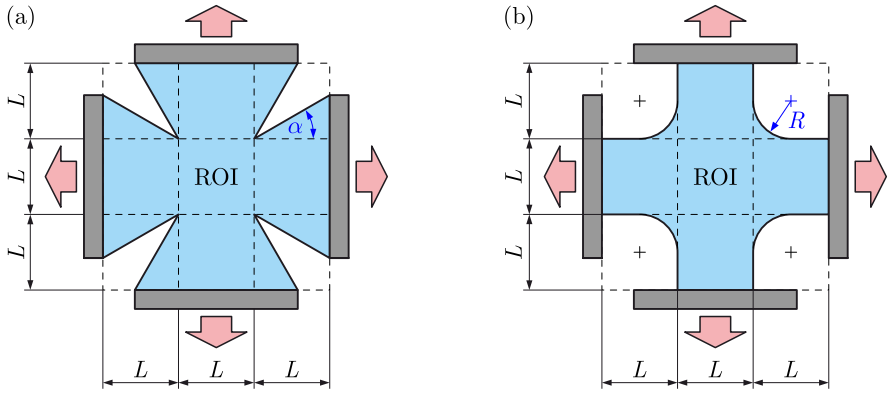

Fig. 2. The two examined geometrical configurations.

Table 1. Coding of the analyzed cases and their corresponding geometric parameters.

Case code	α [°]	Case code	$\beta = R/L$ [1]
A00	0	B01	0.1
A05	5	B02	0.2
A10	10	B03	0.3
A15	15	B04	0.4
A20	20	B05	0.5
A25	25	B06	0.6
A30	30	B07	0.7
A35	35	B08	0.8
A40	40	B09	0.9
A45	45	B10	1.0

The specimens are subjected to identical elongations in the horizontal and vertical directions. Due to the geometrical design, a non-homogeneous stress state develops within the specimens,

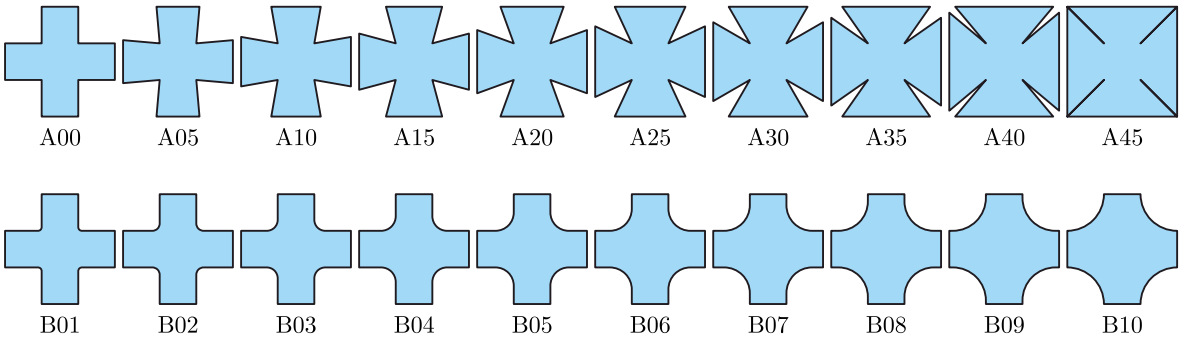

Fig. 3. Illustration of the 20 different geometries analyzed.

and only a single material point (located at the center of the specimen) experiences a purely equibiaxial stress state. Our objective is to determine how the geometrical configuration affects the stress distributions and how the equibiaxial stress-strain relationship, characteristic of the base material, can be extracted from the non-homogeneous stress state. To address these questions, finite element analyses are conducted. The finite element model is described in detail in the following section.

3. Finite element models

Since the aim is to examine purely elastic material behavior, the mechanical behavior of the test specimens is modeled using a hyperelastic material model. The theoretical framework of hyperelastic material modeling is extensively described in various textbooks and scientific articles (Holzapfel, 2010). Due to space constraints, this paper does not provide a detailed presentation of all equations; only the most essential relationships necessary for understanding the results are presented. For isotropic material behavior, the strain energy potential can be expressed using the principal stretches: $U = U(\lambda_1, \lambda_2, \lambda_3)$. The principal stretches are the eigenvalues of the left stretch tensor ($\mathbf{V}$) and the right stretch tensor ($\mathbf{U}$), which can be determined via the polar decomposition of the deformation gradient: $\mathbf{F} = \mathbf{RU} = \mathbf{VR}$. In the case of compressible materials, the Cauchy stress tensor is calculated as follows:

$$\boldsymbol{\sigma} = \sum_{i=1}^{3} \sigma_i \mathbf{n}_i \otimes \mathbf{n}_i = \sum_{i=1}^{3} \frac{\lambda_i}{J} \frac{\partial U}{\partial \lambda_i} \mathbf{n}_i \otimes \mathbf{n}_i, \tag{3.1}$$

where $J = \det\mathbf{F}$ represents the volume ratio, and $\mathbf{n}_i$ $(i = 1, 2, 3)$ are unit vectors in the principal directions of the current configuration. For incompressible materials ($J = 1$), the hydrostatic stress component cannot be determined from the displacement field. In this case, the Cauchy stress tensor is expressed as

$$\boldsymbol{\sigma} = \operatorname{dev}\left[\sum_{i=1}^{3} \lambda_i \frac{\partial U}{\partial \lambda_i} \mathbf{n}_i \otimes \mathbf{n}_i\right] + \mathbf{p}, \tag{3.2}$$

where $\mathbf{p}$, the hydrostatic stress, is determined based on the boundary conditions of the specific problem. In our computations, we employ the Ogden incompressible hyperelastic material model, where the strain energy potential is defined as

$$U = \sum_{i=1}^{N} \frac{2\mu_i}{\alpha_i^2} \left(\lambda_1^{\alpha_i} + \lambda_2^{\alpha_i} + \lambda_3^{\alpha_i} - 3\right). \tag{3.3}$$

Note that the U function presented here corresponds to the version used by Abaqus (Dassault Systèms, 2022). The model's analytical stress solutions for uniaxial, equibiaxial, and planar loading conditions are given by the relations (Steinmann *et al.*, 2012):

$$P_{\text{uniaxial}}(\lambda) = \sum_{i=1}^{N} \frac{2\mu_i}{\alpha_i}\left(\lambda^{\alpha_i-1} - \lambda^{-\alpha_i/2-1}\right),$$

$$P_{\text{equibiaxial}}(\lambda) = \sum_{i=1}^{N} \frac{2\mu_i}{\alpha_i}\left(\lambda^{\alpha_i-1} - \lambda^{-2\alpha_i-1}\right), \tag{3.4}$$

$$P_{\text{planar}}(\lambda) = \sum_{i=1}^{N} \frac{2\mu_i}{\alpha_i}\left(\lambda^{\alpha_i-1} - \lambda^{-\alpha_i-1}\right).$$

For the analysis presented in this manuscript, a third-order Ogden model was fitted to the Treloar data, which are among the most frequently cited experimental datasets in (Treloar, 1944; Steinmann *et al.*, 2012). During the fitting process, only values of $\lambda \leq 5$ were considered. Parameter fitting was conducted using the Wolfram Mathematica built-in NMinimize function to minimize the relative error. The fitted model parameters are as follows:

$$\begin{aligned} &\mu_1 = 0.0309526\,\text{MPa}, && \mu_2 = 0.352102\,\text{MPa}, && \mu_3 = 0.00646444\,\text{MPa}, \\ &\alpha_1 = 3.61341, && \alpha_2 = 0.871956, && \alpha_3 = -2.18698. \end{aligned} \tag{3.5}$$

The comparison between the fitted model and the experimental data is presented in Fig. 4b. The results show that the fitted model is accurate and closely follows the experimental data. The coefficient of determination (R^2) for the fit is 0.999471. A Drucker stability analysis was conducted for the fitted hyperelastic model using the Abaqus built-in module. The results indicate that the hyperelastic model is stable across the entire range.

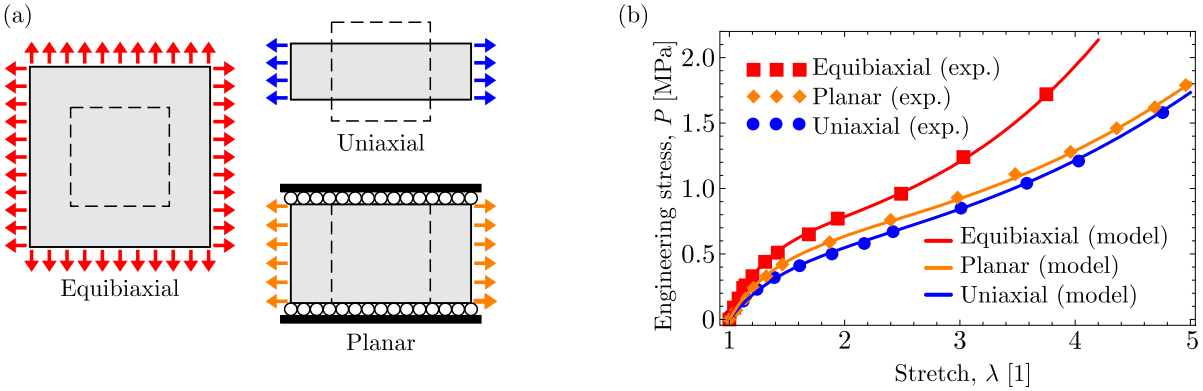

Fig. 4. (a) Illustration of homogeneous loading modes; (b) comparison of experimental data and the model for each loading case.

The finite element simulations were performed using Abaqus software. The test specimens were discretized using 8-node biquadratic plane stress quadrilateral elements (CPS8) with full integration scheme. Note that for plane stress element types, hybrid elements are not required to model incompressible material behavior. Prior to selecting the finite element meshes for analysis, a detailed mesh-independence study was conducted. A global element size was chosen such that the numerical results converged. Due to the symmetry of the geometries, only a quarter of each specimen was modeled with appropriate symmetric boundary conditions. While it would be possible to use an eighth model, for convenience, we opted for the quarter model, as it simplifies the application of boundary conditions. For all geometries, $L = 100\,\text{mm}$ was used with a global element size of 1 mm. To illustrate the finite element meshes, two cases are presented in Fig. 5. The codes shown in the figure correspond to those in Table 1. For these example cases, the number of elements and nodes are as follows: case A20: 16,616 elements and 50,511 nodes; case B05: 14,756 elements and 44,871 nodes.

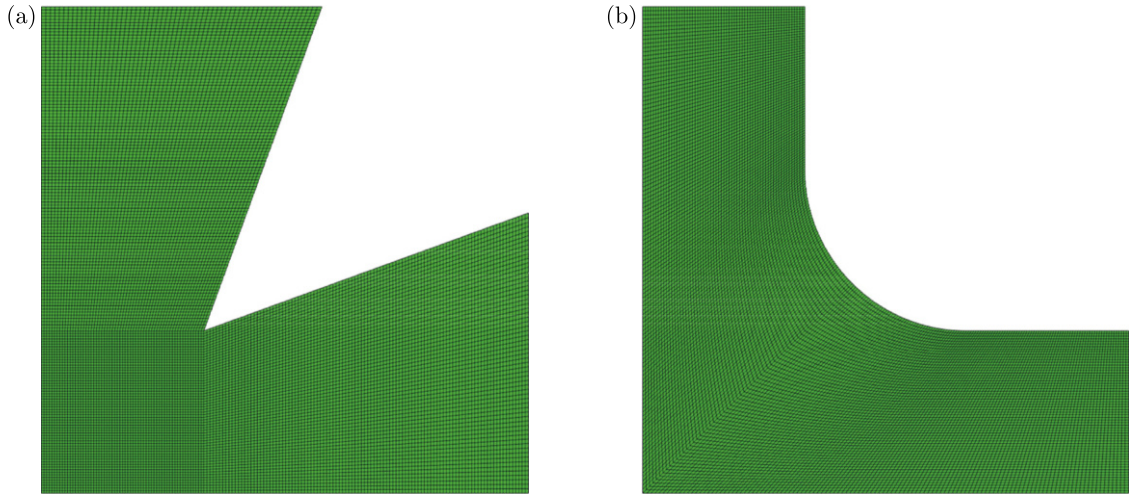

Fig. 5. Finite element meshes applied to the quarter models:
(a) geometry with A20 code; (b) geometry with B05 code.

The prescribed load was applied as displacements at the grips in the horizontal and vertical directions, based on the part of the specimen considered. Displacements perpendicular to the prescribed displacement were constrained, simulating ideal clamping conditions. A displacement value of $u = 600\,\text{mm}$ was prescribed at the grips. At this magnitude, sufficiently large deformations are expected for all geometries. The applied boundary conditions are illustrated schematically in Fig. 6.

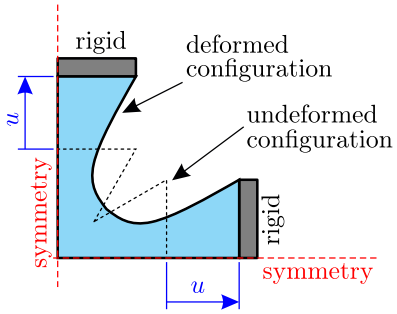

Fig. 6. Schematic illustration of the applied boundary conditions.

The problem was solved using the General Static procedure. The total load was applied in 500 equal increments, providing a sufficiently dense load distribution and reducing numerical errors. During the simulations, reaction forces at the grips were recorded to compute apparent stress values. Let $F/2$ denote the reaction force at the grips in the quarter model. For the investigated loading and geometries, an apparent stretch and nominal stress can be defined as follows:

$$\lambda = 1 + \frac{2u}{3L}, \qquad P = \frac{F}{Lt}, \tag{3.6}$$

where t is the thickness of the specimen. The resulting stretch and nominal stress values correspond to non-purely biaxial stress states, incorporating the influence of geometry. Plotting the nominal stress (P) as a function of λ reveals deviations from the purely equibiaxial solution valid for the material model. To characterize these deviations, a dimensionless stress ratio (or geometry factor) can be introduced:

$$\eta(\lambda) = \frac{P_{\text{equibiaxial}}(\lambda)}{P(\lambda)}. \tag{3.7}$$

The resulting stress ratio (or geometry factor) reflects the influence of geometry on the stress distribution. Knowing η, the purely equibiaxial stress solutions can be computed by multiplying

the measured P values by η. The solutions for each geometry are presented in the following section.

4. Results

First, we present the deformed configurations corresponding to each geometry at the end of loading in Fig. 7. Notably, despite the significant differences in initial configurations, the deformed shapes at the end of the applied large deformation appear very similar. More important than examining the deformed shapes is the variation in reaction forces and the apparent nominal stresses calculated from them. The engineering stress values computed for each specimen are presented in Fig. 8, with different cases distinguished by various colors. The figure also includes the stress solution derived under purely equibiaxial loading conditions, as per Eq. $(3.4)_2$.

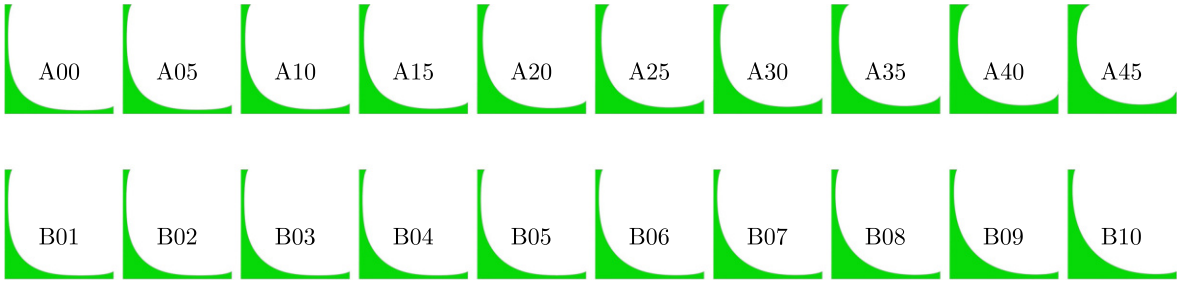

Fig. 7. Deformed configurations obtained for the analyzed geometries.

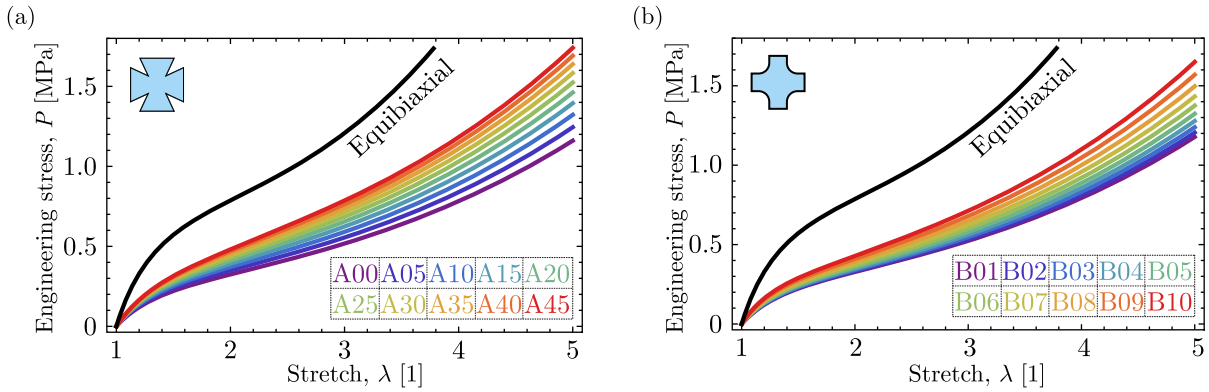

Fig. 8. Plots of the calculated stress values: (a) geometry with A coding; (b) geometry with B coding.

Using these stress solutions, we can compute the variation of the previously introduced η stress ratio as a function of λ. The results are shown in Fig. 9. Analyzing the results reveals that the geometry of the specimen has a significant impact on the value of the stress ratio.

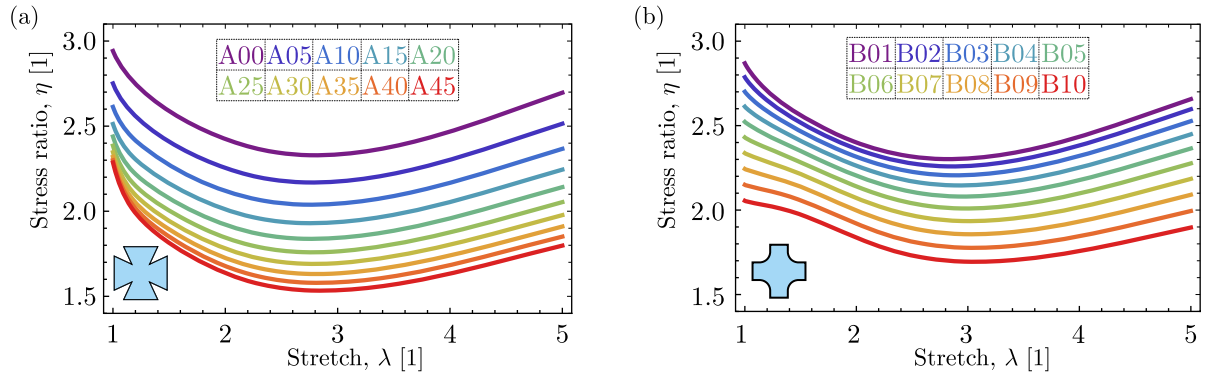

Fig. 9. Plots of the η stress ratio: (a) geometry with A coding; (b) geometry with B coding.

In all cases, the stress ratio depends on the stretch (λ) and consistently falls within the range of 1.5 to 3. If necessary, analytical functions can be fitted to the numerical values of η, but this aspect is beyond the scope of the present paper.

5. Conclusions

In this study, we present a comprehensive analysis of the influence of specimen geometry on the non-homogeneous stress state that develops during biaxial testing of rubber-like materials. Using finite element analysis, we examined a total of 20 configurations based on two characteristic geometries, modeling the base material with a third-order Ogden hyperelastic material model. Apparent stretch and nominal stress quantities were introduced, which can be directly calculated from the crosshead displacement and the measured force. We defined the dimensionless stress ratio, which is the ratio of the stress under purely equibiaxial loading of the base material to the apparent stress, interpreting it as a geometry-specific geometry factor. The stress ratio was calculated for all examined geometries. With the knowledge of the stress ratio, the mechanical behavior of the base material under purely equibiaxial loading conditions can be estimated for various geometries. The presented methodology is extendable to other geometries and materials.

Acknowledgments

This research was supported by the Hungarian National Research, Development and Innovation Office (FK 142457). This research was supported by the János Bolyai Research Scholarship of the Hungarian Academy of Sciences.

References

1. Avanzini, A., & Battini, D. (2016). Integrated experimental and numerical comparison of different approaches for planar biaxial testing of a hyperelastic material. *Advances in Materials Science and Engineering*, *2016*(1), Article 6014129. https://doi.org/10.1155/2016/6014129
2. Bertin, M., Hild, F., Roux, S., Mathieu, F., Leclerc, H., & Aimedieu, P. (2015). Integrated digital image correlation applied to elasto-plastic identification in a biaxial experiment. *Journal of Strain Analysis for Engineering Design*, *51*(2), 118–131. https://doi.org/10.1177/0309324715614759
3. Chen, S., Cai, D., Jiang, H., Li, G., & Cui, J. (2023). A new measurement technology for forming limit in aluminum alloy under biaxial dynamic loading. *Journal of Materials Processing Technology*, *317*, Article 117963. https://doi.org/10.1016/j.jmatprotec.2023.117963
4. Chen, Z., Scheffer, T., Seibert, H., & Diebels, S. (2013). Macroindentation of a soft polymer: Identification of hyperelasticity and validation by uni/biaxial tensile tests. *Mechanics of Materials*, *64*, 111–127. https://doi.org/10.1016/j.mechmat.2013.05.003
5. Dassault Systèmes, 2022, Abaqus version 2022.
6. Hamdoun, A., & Mahnken, R. (2024). Uniaxial and biaxial experimental investigation of glassy polymers. *Polymer*, *299*, Article 126981. https://doi.org/10.1016/j.polymer.2024.126981
7. Hartmann, S., Gilbert, R.R., & Sguazzo, C. (2018). Basic studies in biaxial tensile tests. *GAMM – Mitteilungen*, *41*(1), Article e201800004. https://doi.org/10.1002/gamm.201800004
8. Holzapfel, G.A. (2010). *Nonlinear solid mechanics: A continuum approach for engineering*, Wiley.
9. Jiang, M., Dai, J., Dong, G., & Wang, Z. (2022). A comparative study of invariant-based hyperelastic models for silicone elastomers under biaxial deformation with the virtual fields method. *Journal of the Mechanical Behavior of Biomedical Materials*, *136*, Article 105522. https://doi.org/10.1016/j.jmbbm.2022.105522
10. Kuwabara, T., Ikeda, S., & Kuroda, K. (1998). Measurement and analysis of differential work hardening in cold-rolled steel sheet under biaxial tension. *Journal of Materials Processing Technology*, *80–81*, 517–523. https://doi.org/10.1016/S0924-0136(98)00155-1

11. Labus, K.M., & Puttlitz, C.M. (2016). An anisotropic hyperelastic constitutive model of brain white matter in biaxial tension and structural–mechanical relationships. *Journal of the Mechanical Behavior of Biomedical Materials*, *62*, 195–208. https://doi.org/10.1016/j.jmbbm.2016.05.003

12. Lamkanfi, E., Van Paepegem, W., & Degrieck, J. (2015). Shape optimization of a cruciform geometry for biaxial testing of polymers. *Polymer Testing*, *41*, 7–16. https://doi.org/10.1016/j.polymertesting.2014.09.016

13. Makinde, A., Thibodeau, L., & Neale, K.W. (1992). Development of an apparatus for biaxial testing using cruciform specimens. *Experimental Mechanics*, *32*(2), 138–144. https://doi.org/10.1007/BF02324725

14. Marano, C., Calabrò, R., & Rink, M. (2010). Effect of molecular orientation on the fracture behavior of carbon black-filled natural rubber compounds. *Journal of Polymer Science. Part B: Polymer Physics*, *48*(13), 1509–1515. https://doi.org/10.1002/polb.22054

15. Morris, K., Rosenkranz, A., Seibert, H., Ringel, L., Diebels, S., & Talke, F.E. (2020). Uniaxial and biaxial testing of 3D printed hyperelastic photopolymers. *Journal of Applied Polymer Science*, *137*(8), Article 48400. https://doi.org/10.1002/app.48400

16. Oliveira, M.G., Thuillier, S., & Andrade-Campos, A. (2021). Evaluation of heterogeneous mechanical tests for model calibration of sheet metals. *The Journal of Strain Analysis for Engineering Design*, *57*(3), 208–224. https://doi.org/10.1177/03093247211027061

17. Palacios-Pineda, L., Perales-Martínez, I., Moreno-Guerra, M., & Elías-Zúñiga, A. (2017). An optimum specimen geometry for equibiaxial experimental tests of reinforced magnetorheological elastomers with iron micro- and nanoparticles. *Nanomaterials*, *7*(9), Article 254. https://doi.org/10.3390/nano7090254

18. Putra, K.B., Tian, X., Plott, J., & Shih, A. (2020). Biaxial test and hyperelastic material models of silicone elastomer fabricated by extrusion-based additive manufacturing for wearable biomedical devices. *Journal of the Mechanical Behavior of Biomedical Materials*, *107*, Article 103733. https://doi.org/10.1016/j.jmbbm.2020.103733

19. Ranjan, R., Murthy, H., Bhowmik, D., & Sadavarte, V.S. (2023). Behaviour of composite solid propellant under biaxial tensile loading. *Polymer Testing*, *124*, Article 108054. https://doi.org/10.1016/j.polymertesting.2023.108054

20. Seibert, H., Scheffer, T., & Diebels, S. (2014). Biaxial testing of elastomers – experimental setup, measurement and experimental optimisation of specimen's shape. *Technische Mechanik*, *34*(2), 72–89. https://doi.org/10.24352/UB.OVGU-2017-054

21. Silberstein, M.N., Pillai, P.V., & Boyce, M.C. (2011). Biaxial elastic–viscoplastic behavior of Nafion membranes. *Polymer*, *52*(2), 529–539. https://doi.org/10.1016/j.polymer.2010.11.032

22. Steinmann, P., Hossain, M., & Possart, G. (2012). Hyperelastic models for rubber-like materials: consistent tangent operators and suitability for Treloar's data. *Archive of Applied Mechanics*, *82*(9), 1183–1217. https://doi.org/10.1007/s00419-012-0610-z

23. Treloar, L.R.G. (1944). Stress-strain data for vulcanized rubber under various types of deformation. *Rubber Chemistry and Technology*, *17*(4), 813–825. https://doi.org/10.5254/1.3546701

24. Vitucci, G. (2024). Biaxial extension of cruciform specimens: Embedding equilibrium into design and constitutive characterization. *Experimental Mechanics*, *64*(4), 539–550. https://doi.org/10.1007/s11340-024-01052-2

25. Zhao, X., Berwick, Z.C., Krieger, J.F., Chen, H., Chambers, S., & Kassab, G.S. (2014). Novel design of cruciform specimens for planar biaxial testing of soft materials. *Experimental Mechanics*, *54*(3), 343–356. https://doi.org/10.1007/s11340-013-9808-4

Manuscript received December 3, 2024; accepted for publication February 11, 2025; published online May 17, 2025.